https://doi.org/10.5194/ar-2025-34
Preprint. Discussion started: 7 November 2025

AEROSOL Research Discussions

Characterizing aerosol sources based on aerosol optical properties and dispersion modelling in a Scandinavian Coastal Area (Aarhus, Denmark)

Zihui Teng[1,*], Jane Tygesen Skønager[1,*], Andreas Massling[2], Henrik Skov[2], Nikolaos Evangeliou[3], Sabine Eckhardt[3], Merete Bilde[1], and Bernadette Rosati[1,4]

[1]Department of Chemistry,Aarhus,University,Aarhus, 8000, Denmark
[2]Department of Environmental Science, iClimate, ARC, Aarhus University, Roskilde, 4000, Denmark
[3]Stiftelsen NILU (former Norwegian Institute for Air Research), Kjeller, 2007, Norway
[4]Institute of Meteorology and Climatology, University of Natural Resources and Life Sciences, Vienna, 1180, Austria
[*]These authors contributed equally to this work.

Correspondence: Bernadette Rosati (bernadette.rosati@boku.ac.at)

Abstract. Coastal aerosols are formed through the complex mixing between marine air masses and continental emissions, which originate from both natural and anthropogenic sources. The properties of coastal aerosols are decisive for their interaction with sunlight and influence on clouds as well as the potential health implications for the population in these areas. In this study, the aerosol properties and sources at Aarhus Bay, Denmark, were investigated by combining in-situ aerosol light scattering and absorption with size distribution measurements and footprint analysis by FLEXPART. Our analysis demonstrates a considerable contribution of anthropogenic aerosols from both fossil fuel combustion and biomass burning as well as periods with highly scattering aerosols. Furthermore, good agreement was found between in-situ and modelled black carbon data. Combining in-situ measurements and FLEXPART analysis further evidenced a major impact of local emissions as well as a few long-range transport intrusions.

1 Introduction

Atmospheric aerosols play a critical role in regional and global climate systems by scattering and absorbing solar radiation and by acting as nuclei for cloud droplets and ice crystals (Masson-Delmotte et al., 2021). Despite their importance, aerosol-radiation and aerosol-cloud interactions remain among the largest sources of uncertainty in current climate predictions (Masson-Delmotte et al., 2021). At the same time aerosols can have negative impacts on human health (Pope III and Dockery, 2006). Reducing uncertainties on aerosol climate effects and improving insights into aerosol adverse health effects require knowledge about ambient aerosol loading and properties across diverse environments. Coastal regions are particularly complex environments where marine and continental air masses interact, leading to highly variable aerosol chemical composition and physical properties (Lewis and Schwartz, 2004). Coastal airmasses are influenced by both anthropogenic and natural sources, including contributions from sea spray, shipping, urban outflow, and biogenic activity. Importantly, coastal zones are also home to a large fraction of the global population, as approximately 40 % of people live within 100 km of a coastline (Cosby et al.,

https://doi.org/10.5194/ar-2025-34
Preprint. Discussion started: 7 November 2025

2024), highlighting the importance of understanding aerosol characteristics in these regions for air quality and human health purposes.

The interaction of aerosol particles and solar radiation depends on particle size, shape, and chemical composition as well as the incident wavelengths (Bohren and Huffman, 2008). These are determined by the aerosols' sources and how they have been processed in the atmosphere. In-situ measurements of scattering and absorption coefficients and derived quantities like single scattering albedo and Ångström exponents provide a direct way to probe these characteristics (Cazorla et al., 2013; Cappa et al., 2016; Dubovik et al., 2002). The wavelength dependence of the optical parameters allows to distinguish between particle types such as dust, black carbon (BC), and brown carbon (BrC). Coupling these measurements with auxiliary in-situ data, such as particle size distributions, and airmass back trajectories further constrains source regions thereby enhancing our ability to trace observed aerosol variability back to particular emission sources and transport pathways.

Several long-term atmospheric monitoring stations have provided valuable insights into aerosol behaviour in coastal and marine-influenced environments. Sites such as Mace Head (Ireland), Finokalia (Greece), and the Cape Verde Atmospheric Observatory have contributed decades of in-situ data on aerosol optical, chemical, and microphysical properties (e.g. Dall'Osto et al., 2010; Kalivitis et al., 2019; Fomba et al., 2014). While aerosol optical properties have been widely studied using remote sensing techniques (e.g. Zhang et al., 2025) only a handful of shorter field campaigns have examined the scattering and absorption potential of ambient aerosols particularly in Scandinavia (Ahlberg et al., 2023; Martinsson et al., 2014; Mogo et al., 2012), and only few targeted coastal aerosols (Mogo et al., 2012; Clarke et al., 2003; Donateo et al., 2020). Although Denmark has a long coastline compared to the size of the country (Worm, 1997), studies of coastal aerosols in Denmark are scarce (Vignati et al., 1999; Kivekäs et al., 2014), and none have coupled aerosol optical properties with size-distribution measurements and trajectory modelling, limiting our understanding on source attribution and radiative impacts in these settings.

In this study, we measured and analysed the absorption and scattering potential as well as number and surface size distributions of aerosols measured at a coastal site in Denmark during a 6.5-week field campaign in spring 2023. Our site was located near Aarhus, at the Kattegat coast of Jutland in Denmark,offering a unique environment to study the properties of coastal aerosols. Depending on wind direction and synoptic conditions, this site can be influenced by marine air masses from the North Sea or the Baltic Sea, long-range transported aerosols from continental Europe and Asia as well as local influences such as emissions from nearby shipping lanes and urban outflow from the city of Aarhus.

The wavelength dependence of these optical parameters, combined with number and surface size distribution data, was used to assess aerosol types and sources. To further investigate source regions and particle age, we employed the Lagrangian particle dispersion model FLEXPART to simulate air mass histories. Within specific case studies we highlight the variability in aerosol loading and composition. The results contribute to a more detailed understanding of aerosol sources and their characteristics in coastal Denmark.

https://doi.org/10.5194/ar-2025-34
Preprint. Discussion started: 7 November 2025

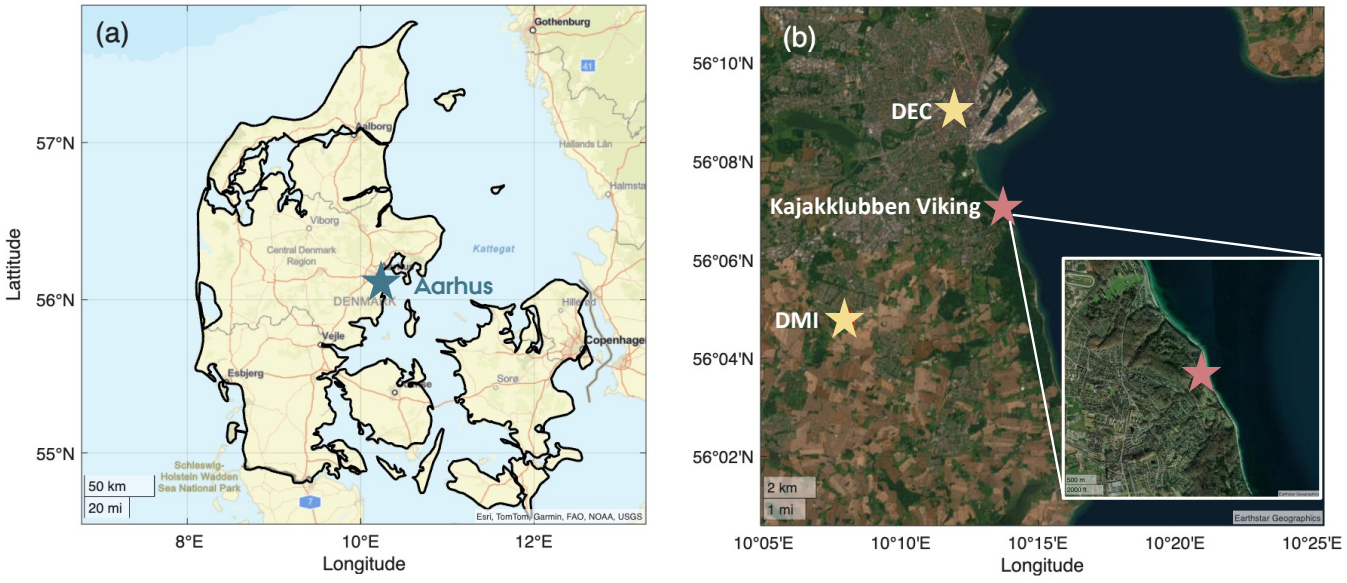

Figure 1. Map of (a): Aarhus (Basemap Sources: Esri, TomTom, Garmin, FAO, NOAA, USGS) and (b): sampling sites (Basemap provided by Earthstar Geographics.). In (b), Kajakklubben Viking is marked with a red star and DMI and DCE stations providing meteorological and air quality data are marked with yellow stars. It was Produced using MATLAB version 9.14 (R2023a). (Matlab, 2021).

2 Methods

2.1 Measurement site

The measurements were carries out in Aarhus (56.13° N, 10.22° E) from 3 March to 11 April, 2023. Aarhus is a coastal city, the second largest city in Denmark, and has approximately 360.000 inhabitants and an area of 468 km^2. As shown in Fig.1, the instruments were placed in the house of a Kayak club ("Kajakklubben Viking"), located on a beach along the southeastern coastline of Aarhus. The coastline is boarded by a forest area, where there is a habitat for a herd of deer. Outside the forest, there are main roads, residential houses and agricultural fields (to the south-west). In addition, Aarhus Port, one of Denmark's largest container ports, is at a distance of 3.83 km from the sampling site (to the north). Thus, the measurement site is potentially influenced by clean marine, forest and anthropogenic emissions from residential activities, traffic both from the continent (i.e. vehicles) and the sea (marine shipping).

Wind, radiation and relative humidity (RH) data were obtained from the Danish Meteorological Institute (DMI). The closest DMI measurement site is located in the south of Aarhus (56.1° N, 10.23° E), 7 km from the Kayak club. PM_{10} (particulate matter with a diameter of less than 10 µm), nitrous oxide (NO_x) and carbon monoxide (CO) were monitored by the Danish Center for Environment and Energy (DCE), from a station about 5 km from the Kayak Club, located at Banegårdsgade (56.15° N, 10.20° E), close to the railway station characterized by heavy traffic (Nordstrøm et al., 2024).

https://doi.org/10.5194/ar-2025-34
Preprint. Discussion started: 7 November 2025

AEROSOL Research Discussions

2.2 Instrumentation

A nephelometer (Aurora 3000, Ecotech), an aethalometer (AE33, Aerosol Magee Scientific) and a white-light optical particle spectrometer (Welas® 2300, PROMO 3000, PALAS) were used to obtain the scattering and absorption coefficients as well as the number ans surface particle size distributions of the aerosols. The three instruments were placed inside "Kajakklubben Viking" and shared a stainless steel inlet via a three-way splitter to separate the airflow. The inlet was installed through the wall, parallel to the ground, at a height of around 4 m above the beach. A steel net covered the end of the inlet to prevent droplets and bugs from entering the inlet. A schematic is presented in Fig. S1.

The nephelometer measured the integrating intensity of total light scattering and backscattering from aerosols and gas molecules at three wavelengths (λ = 470 nm, 525 nm, and 630 nm) with a resolution of 1 minute. The data were corrected for angular truncation errors according to Müller et al. (2011). The nephelometer operated at a flow rate of 5.0 L min_{-1}. Both total scattering (angles between 10° and 171°) and backscattering (angles between 90° to 171°) were measured. A full calibration, including zero measurement and span gas calibration with carbon dioxide (CO_2) (99.9 % purity), was performed prior to the measurements. The nephelometer was equipped with a RH sensor in the measurement cell and two temperature sensors, one in the inlet and the other one in the measurement cell.

The aethalometer measured light attenuation at 7 wavelengths (λ = 370 nm, 470 nm, 520 nm, 590 nm, 660 nm, and 880 nm) at 1 minute time resolution and a flow rate of 5 L min_{-1} (Drinovec et al., 2015). The absorption coefficients are related to the equivalent black carbon (eBC) mass concentrations and are calculated using Eq. (1), where MAC is the mass absorption cross section (Hansen et al., 1984):

$$\sigma_{abs}(\lambda) = eBC(\lambda) \cdot MAC(\lambda) \quad (1)$$

A MAC value of 7.77 (m^2 g^{-1}) was used for λ = 880 nm, as suggested in the manual. This value was previously deployed for aerosols measured in southern Sweden (Ahlberg et al., 2023). Black carbon source apportionment, to subdivide the fractions from fossil fuel combustion and biomass burning, was performed according to Sandradewi et al. (2008), where the portion from biomass burning is referred to as BB%. There is a multiple scattering effect caused by light scattering between the particles and the filter fibres. It depends on both the type of filter and the single scattering albedo of the aerosol. Therefore, we followed the approach by Drinovec et al. (2015) including the single scattering albedo of aerosol to improve the correction factor value of 1.57 for TFE-coated glass filter (M8020) tape for the aethalometer. Using a maximum value of 0.025 for the cross-sensitivity of absorption to scattering, as stated in (Drinovec et al., 2015), we find that the maximum total correction factors for both scattering from the aerosol and the filter fibres were 1.76, 1.77, and 1.79 for λ = 470 nm, 520 nm and 660 nm. This results in a maximum relative error on the absorption coefficients due to the scattering of the particles of up to 12.25 %, 12.99 % and 14.47 % for λ = 470 nm, 520 nm and 660 nm, respectively. This indicates that the scattering by the aerosols in our specific case did not have a significant effect on the measured absorption signal.

The white-light optical particle spectrometer WELAS was used to measure number and surface size distributions of particles with optical diameters from approximately 0.2 µm to 10 µm (in polystyrene latex (PSL) equivalent particle diameters). A flow

https://doi.org/10.5194/ar-2025-34
Preprint. Discussion started: 7 November 2025

AEROSOL Research Discussions

rate of 5 L min_{-1} was used. The WELAS sensors were calibrated with MonoDust 1500 as provided by PALAS prior to the measurements.

Prior to data processing, all raw data were cleaned for instances with RH above 40 %, tubing disconnection and tape advancement of the aethalometer.

2.3 Inlet and sampling efficiency calculation

A schematic illustrating the tubing used for the inlet and instrumental setup at the measurement site are presented in Fig. S1. To assess losses of particles in the sampling probe and inlet tubing, we calculated overall inlet efficiency as a function of particle diameter using an open-source particle loss calculator (von der Weiden et al., 2009). This was done for each instrument by inputting length, diameter, angle of inclination, angle of curvature, and sample flow for each tubing piece between the instrument and the sampling inlet. For all three instruments we found decreasing inlet efficiencies with increasing particle size. The nephelometer and aethalometer have a 50 % inlet efficiency for a particle diameter of 8 μm , whereas the WELAS has a 50 % inlet efficiency for a particle diameter of approximately 6.5 μm. We also calculated the sampling efficiency of the sampling probe at five different wind speeds: 0 m s^{-1}, 2.5 m s^{-1}, 5 m s^{-1}, 7.5 m s^{-1} and 10 m s^{-1}. At wind speeds 0 and 2.5 m s^{-1} there is a depletion in the sampling efficiency of larger particles, whereas at wind speeds 7.5 and 10 m s^{-1}, there is an enrichment in the sampling efficiencies of larger particles. Efficiency curves are presented in Fig. S2 and tubing parameter tables in Tables S1-S3.

2.4 Optical parameters

The Single Scattering Albedo (SSA), Absorption Ångström Exponent (AAE), Scattering Ångström Exponent (SAE), spectral variation of SAE (ΔSAE), backscattering ratio (b) and asymmetry parameter (g) were derived from the scattering and absorption coefficients measured by the nephelometer and aethalometer.

SSA was calculated using Eq. (2) as the ratio of scattering coefficient (σ_{sca}) to extinction coefficient, which is the sum of the scattering coefficient and absorption coefficient (σ_{abs}). SSA values at wavelengths (λ) of 470 nm, 520 nm, 660 nm were calculated; thus the scattering coefficients were recalculated for these three wavelengths based on a power law fitting (Ångström, 1929).

$$SSA(\lambda) = \frac{\sigma_{sca}(\lambda)}{\sigma_{sca}(\lambda) + \sigma_{abs}(\lambda)} \tag{2}$$

Typical values of SSA for sea salt and sulfate aerosol are expected to be close to 1 at λ = 550 nm (Takemura et al., 2002), while fresh BC is highly absorbing and has been shown to have SSA values close to 0.3 at λ = 554 nm (Bergstrom et al., 2002).

SAE and AAE reflect the spectral variability of light scattering and absorption and were found using Eq. (3) and Eq. (4). SAE was derived from the wavelength pair of 450 nm and 550 nm to compare to Cappa et al. (2016). Values that were not directly measured, were recalculated based on power-law fitting.

https://doi.org/10.5194/ar-2025-34
Preprint. Discussion started: 7 November 2025

AEROSOL Research Discussions

$$SAE(450nm, 550nm) = -\frac{ln[\sigma_{sca}(450nm)/\sigma_{sca}(550nm)]}{ln(450nm/550nm)} \quad (3)$$

$$AAE(532nm, 660nm) = -\frac{ln[\sigma_{abs}(532nm)/\sigma_{abs}(660nm)]}{ln(532nm/660nm)} \quad (4)$$

SAE is inversely related to particle size: aerosol particles typically found in the coarse mode, such as dust, pollen and sea salt, have been reported to show SAE values of 0.5 (Costabile et al., 2013), while small particles such as carbonaceous particles originating from fossil fuel combustion or biomass burning, have typical SAE values greater than 1.5 (Cazorla et al., 2013). AAE is related to the chemical composition of the particles: BC is known to absorb radiation equally well at all wavelengths, thus having AAE values close to 1 (Bond and Bergstrom, 2006), while dust (e.g. from soil or volcanic eruptions) and brown carbon (BrC; from biomass burning) show a wavelength dependency with higher absorption in the ultraviolet and blue spectral regions (Kirchstetter et al., 2004) (i.e. AAE $>$ 1.5). Finally, the Ångström matrix, which combines AAE and SAE values, can be subdivided into several regions representative for different aerosol types and sources (Cazorla et al., 2013; Cappa et al., 2016).

ΔSAE describes the spectral variation of SAE, calculated as Perrone et al. (2018):

$$\Delta SAE = SAE(450nm, 550nm) - SAE(550nm, 700nm) \quad (5)$$

While SAE is related to the mean size and relative concentrations of the accumulation and coarse mode aerosol, ΔSAE provides information on the contribution of fine and coarse mode particles leading to a better understanding of the SAE values (Perrone et al., 2018). A negative value indicates a large contribution from a single, fine mode, while a positive value indicates a contribution from both the fine and coarse modes, where higher values represent a larger contribution of the coarse mode particles.

The backscattering ratio, b, is defined as the ratio of backscattering coefficients ($\sigma_{\mathrm{bsca},\lambda}$) to total scattering coefficients ($\sigma_{\mathrm{sca},\lambda}$):

$$b(\lambda) = \frac{\sigma_{bsca}(\lambda)}{\sigma_{sca}(\lambda)} \quad (6)$$

b values range from 0 to 1, where a high fraction of larger particles results in a smaller value of b, as large particles (size larger than wavelength) predominantly scatter radiation in the forward direction (Bohren and Huffman, 2008).

b can also be used to estimate the asymmetry parameter, g (Andrews et al., 2006). g is the cosine-weighted average of the phase function, which describes the angular distribution of the scattered radiation. It ranges from -1 to 1, representing total backscattering and total forward scattering, respectively, whereas 0 represents symmetric scattering. It is a crucial parameter in radiative transfer models, climate models, and general circulation models used to estimate the direct radiative effect of aerosols (Bellouin et al., 2005; Barman et al., 2024). g was calculated using Eq. (7):

$$g = -7.143889 \cdot b_\lambda^3 + 7.464439 \cdot b_\lambda^2 - 3.96356 \cdot b_\lambda + 0.9893 \quad (7)$$

https://doi.org/10.5194/ar-2025-34
Preprint. Discussion started: 7 November 2025

AEROSOL Research Discussions

2.5 Source-receptor modelling with FLEXPART

The origins of the airmasses arriving at the receptor site, where sampling instruments were placed, were simulated with the Lagrangian particle dispersion model FLEXPART version 10.4 (Pisso et al., 2019). The model emits computational particles at the surface that are tracked backward in time by the ambient flow, as defined by meteorological fields that are used as input to the model. In the present study, the meteorological input was based on hourly reanalysis meteorological fields (ERA5) from the European Centre for Medium-Range Weather Forecasts (ECMWF) with 137 vertical levels (up to approximately 80 km) and a horizontal resolution of 0.5°×0.5° (Hersbach et al., 2020). Simulations extended over 30 days backward in time, a sufficient period to capture more than 98 % of most BC emissions arriving at the receptor, given a typical BC lifetime of 1 week (Bond et al., 2013). FLEXPART includes gravitational settling for spherical particles, dry and wet deposition of aerosols (Grythe et al., 2017), turbulence (Cassiani et al., 2015), unresolved mesoscale motions (Stohl et al., 2005), and deep convection (Forster et al., 2007). The model output consists of a footprint emission sensitivity that expresses the probability of any emission occurring in any grid-cell to arrive at the receptor site and can be converted to model concentration, when coupled with gridded emissions.

Anthropogenic emissions were adopted from the latest version (v6b) of the ECLIPSE (Evaluating the CLimate and Air Quality ImPacts of ShortlivEd Pollutants) dataset, an upgraded version of the previous version (Klimont et al., 2017). The inventory includes emissions from industrial combustion (IND), from the energy production sector (ENE), residential and commercial emissions (DOM), emissions from waste treatment and disposal sector (WST), transportation (TRA), shipping activities (SHP) and gas flaring emissions (FLR). The methodology for obtaining emissions from FLR specifically over the Russian territories has been improved in ECLIPSEv6 (Böttcher et al., 2021). Biomass burning (BB) from wildfires was adopted from the Copernicus Global Fire Assimilated System (CAMS-GFAS) (Kaiser et al., 2012), a product that provides estimates of the injection altitude of the fire emissions that is crucial for accurate simulation of the BB dispersion.

3 Results and Discussion

3.1 Main features of optical and physical properties

Figure 2 presents an overview of the aerosol optical properties during the measurement period, each data point represents an average of 10 min, while Table 1 presents numerical values. Figure 2(a) shows scattering coefficients (σ_{sca}) at three different wavelengths. Two periods with particularly high σ_{sca} are visible, the first from 18 to 20 March and the second from 30 to 31 March. Apart from these two periods, the values of σ_{sca} were below 100 Mm^{-1}. The average σ_{sca} at 440 nm, 525 nm and 635 nm were found to be 35.2 Mm^{-1}, 29.0 Mm^{-1} and 23.7 Mm^{-1}, respectively. In addition, the σ_{sca} at 440 nm was generally higher than at 525 nm and 635 nm, indicating that fine-mode particles contributed significantly to the aerosols. The period with the highest absorption coefficients (σ_{abs}) was observed from 17 to 20 March (Fig. 2(b)). Many sharp peaks were only visible in σ_{abs} and were absent in σ_{sca}, indicating the presence of high-absorbing particles for short periods of times. These were likely emitted by traffic or biomass burning near the site. Therefore, they are not considered representative of the regional aerosols. The average σ_{abs} at 370 nm, 470 nm, 520 nm, 590 nm, 660 nm, 880 nm, 950 nm were 7.41 Mm^{-1}, 5.32 Mm^{-1}, 4.53 Mm^{-1},

https://doi.org/10.5194/ar-2025-34
Preprint. Discussion started: 7 November 2025

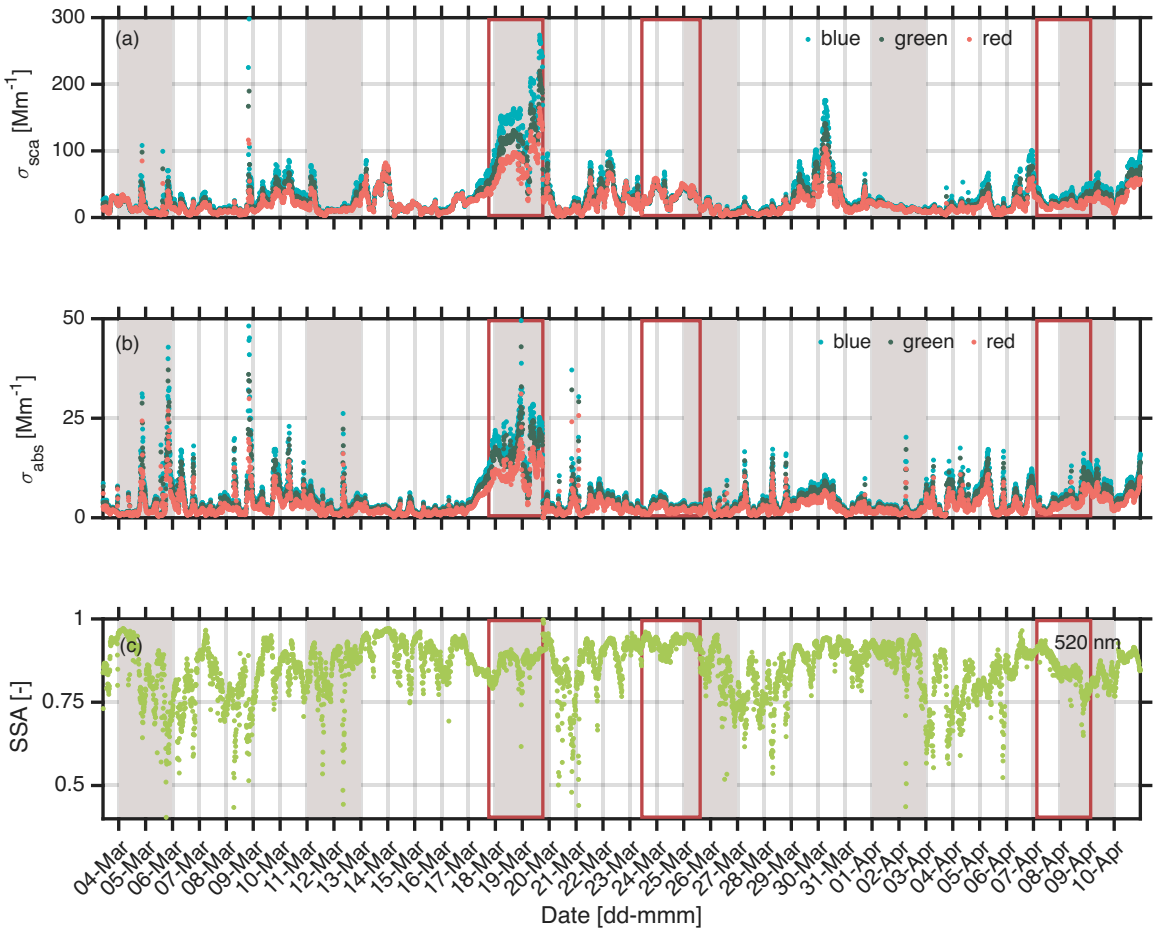

Figure 2. 10 min averages of optical properties during the whole measurement period with weekends highlighted in grey, and the three selected cases highlighted with red squares. (a) scattering coefficient σ_{sca} at three wavelengths (blue: 450 nm, green: 525 nm, red: 635 nm); (b) absorption coefficient σ_{abs} at three wavelengths (blue: 470 nm, green: 520 nm, red: 660 nm); (c) single scattering albedo SSA at 520 nm; σ_{sca} at 520 nm was recalculated using power law fitting.

https://doi.org/10.5194/ar-2025-34
Preprint. Discussion started: 7 November 2025

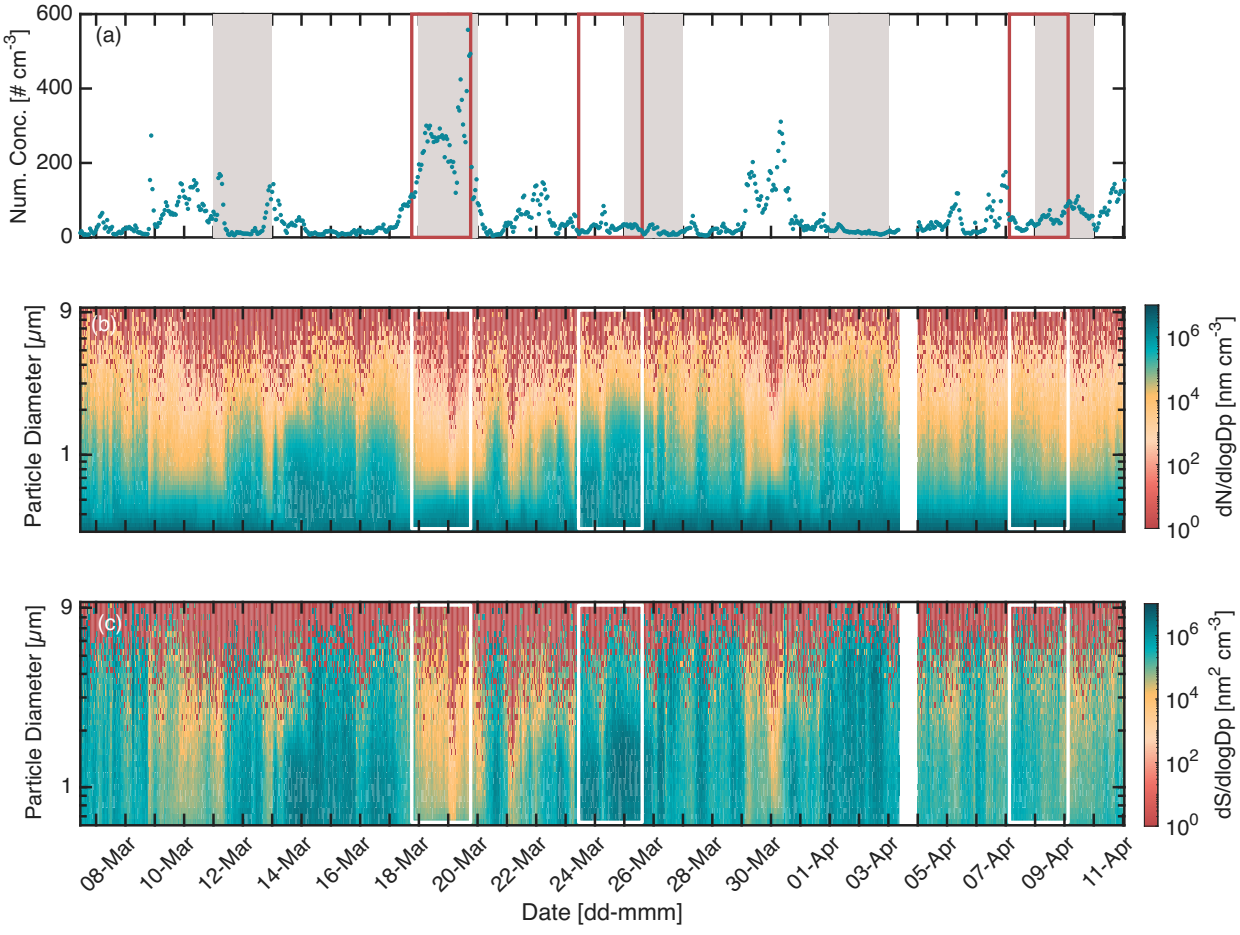

Figure 3. Time series of particle concentration and size distribution during the whole measurement period, with weekends highlighted in grey and the three selected cases with red rectangles. (a) total number concentration N_{TOT}, (b) number size distribution dN/dlogDp, and (c) surface area size distribution dS/dlogDp.

https://doi.org/10.5194/ar-2025-34
Preprint. Discussion started: 7 November 2025

AEROSOL Research Discussions

Table 1. Mean ± standard deviation (median) values of 10 min averaged optical parameters and total number concentration for the whole period (3 March to 11 April) and the three cases.

Parameter	λ(nm)	Whole period	Case 1	Case 2	Case 3
σ_{sca} (Mm^{-1})	450	35.16 ± 34.43 (24.42)	121.19 ± 54.00 (127.92)	35.55 ± 11.30 (35.88)	30.84 ± 8.66 (29.54)
	525	29.02 ± 27.39 (20.24)	96.49 ± 43.01 (99.91)	34.62 ± 10.91 (34.82)	24.46 ± 6.30 (23.40)
	635	23.72± 20.77 (17.29)	71.81 ± 31.57 (73.05)	34.85 ± 11.67 (34.22)	19.14 ± 4.464 (18.85)
σ_{abs} (Mm^{-1})	470	5.32 ± 5.31 (3.61)	17.28 ± 6.23 (17.08)	3.07 ± 1.20 (2.86)	5.66 ± 3.22 (4.92)
	520	4.53 ± 4.43 (3.06)	14.73 ± 5.35 (14.52)	2.64 ± 1.03 (2.47)	4.83 ± 2.66 (4.23)
	660	3.26 ± 3.09 (2.20)	10.49 ± 3.82 (10.33))	1.99 ± 0.74 (1.86)	3.45 ± 1.84 (3.01)
SSA	470	0.85 ± 0.08 (0.87)	0.86 ± 0.04 (0.87)	0.92 ± 0.02 (0.92)	0.84 ± 0.05 (0.84)
	520	0.85 ± 0.08 (0.87)	0.86 ± 0.03 (0.87)	0.93 ± 0.02 (0.93)	0.85 ± 0.05 (0.84)
	660	0.82 ± 0.10 (0.84)	0.81 ± 0.04 (0.82)	0.93 ± 0.03 (0.94)	0.80 ± 0.07 (0.80)
AAE	470/660	1.37 ± 0.26 (1.39)	1.47 ± 0.09 (1.45)	1.25 ± 0.14 (1.27)	1.41 ± 0.15 (1.41)
	532/660	1.41 ± 0.28 (1.41)	1.52 ± 0.13 (1.49)	1.32 ± 0.14 (1.34)	1.44 ± 0.17 (1.42)
SAE	450/635	1.03 ± 0.68 (1.19)	1.50 ± 0.18 (1.51)	0.08 ± 0.44 (-0.07)	1.35 ± 0.33 (1.35)
	450/550	1.15 ± 0.74 (1.32)	1.49 ± 0.22 (1.51)	0.17 ± 0.52 (0.05)	1.46 ± 0.37 (1.48)
Δ SAE	-	0.22 ± 0.42 (0.19)	-0.04 ± 0.21 (-0.07)	0.16 ± 0.33 (0.16)	0.20 ± 0.30 (0.22)
b	450	0.12 ± 0.02 (0.12)	0.11 ± 0.01 (0.10)	0.12 ± 0.01 (0.12)	0.14 ± 0.01 (0.14)
	525	0.13 ± 0.02 (0.13)	0.11 ± 0.01 (0.10)	0.12 ± 0.01 (0.12)	0.15 ± 0.01 (0.15)
	635	0.14 ± 0.02 (0.13)	0.12 ± 0.02 (0.11)	0.11 ± 0.01 (0.11)	0.16 ± 0.01 (0.16)
g	450	0.60 ± 0.04 (0.60)	0.65 ± 0.02 (0.66)	0.61 ± 0.02 (0.61)	0.58 ± 0.02 (0.58)
	525	0.59 ± 0.04 (0.58)	0.63 ± 0.04 (0.65)	0.62 ± 0.01 (0.62)	0.55 ± 0.02 (0.55)
	635	0.58 ± 0.05 (0.58)	0.61 ± 0.04 (0.62)	0.64 ± 0.02 (0.65)	0.53 ± 0.02 (0.52)
eBC (ng m^{-3})	880	317.53 ± 269.97 (231.30)	944.82 ± 346.60 (927.80)	217.49 ± 65.60 (212.55)	337.48 ± 151.33 (294.40)
BB%	-	22.90 ± 11.93 (22.40)	24.97 ± 5.42 (23.89)	15.33 ± 8.31 (13.78)	24.01 ± 9.05 (24.55)
N_{TOT} (# cm^{-3})	-	58.04 ± 70.15 (31.48)	225.53 ± 111.43 (231.77)	29.40 ± 14.27 (27.66)	52.96 ± 22.04 (51.66)

3.86 Mm^{-1}, 3.26 Mm^{-1}, 2.37 Mm^{-1}, 2.22 Mm^{-1}, respectively. In general, the absorption coefficients decreased with increasing wavelengths. Compared to Vavihill, a background site in southern Sweden, mean σ_{sca} values at 525 nm in this study (29.02 ± 27.39 Mm^{-1}) were lower than in the Swedish study, where values amounted to 48.0 ± 44.6 Mm^{-1} for a similar period of the year (1 March - 1 April 2011). Also, mean σ_{abs} values at 520 nm from this study (4.53 ± 4.43 Mm^{-1}) were slightly lower compared to those measured at Vavihill, amounting to 6.1 ± 6.5 Mm^{-1} at 520 nm, for the same season (Roldin, 2012; Genberg, 2012). A follow-up study in Vavihill in April 2013 reported a similar value of approximately 5 Mm^{-1} at 520 nm (Martinsson et al., 2014). Compared to a coastal, Mediterranean city (Lamezia Terme, Italy), characterized by anthropogenic pollution emissions

https://doi.org/10.5194/ar-2025-34
Preprint. Discussion started: 7 November 2025

AEROSOL Research Discussions

related to traffic and agriculture (Donateo et al., 2020), the mean σ_{sca} values at 550 nm during the cold season (October to March from 2015 to 2018) were found higher than those from this study with mean values of 39 Mm^{-1} (Donateo et al., 2020).

A mean eBC value of 318 ± 270 ng m^{-3} was found during the whole measurement period, as calculated from the σ_{abs} value at 880 nm. Furthermore, the mean value of BB%, characterizing the fraction of biomass burning to the eBC load, was 22.9 % with a large standard deviation of 11.9 %. This indicates that biomass burning also contributed significantly to the absorbing aerosols at Aarhus Bay. eBC values at Vavihill, as calculated from presented σ_{abs} values at 880 nm during April 2013, were found to be approximately 380 ng m^{-3} (Martinsson et al., 2014), which is in the same range as our measurements at Aarhus Bay. On the other hand, eBC values in Malmö, a coastal city in southern Sweden with a similar population to Aarhus, were higher with on average about 500 ng m^{-3} in autumn 2018 (Ahlberg et al., 2023). Interestingly, the mean eBC concentration at Lamezia Terme was 690 ng m^{-3} (Donateo et al., 2020) and thus significantly higher than the mean value in Aarhus during the cold season.

Figure 2(c) depicts the single scattering albedo (SSA) at 520 nm, which ranged from 0.28 to 0.99 with a mean and standard deviation of 0.85 ± 0.08. Oceanic aerosols are generally expected to have high SSA values close to 1 at wavelengths from 440 to 1020 nm, while urban aerosols and biomass burning aerosols are typically described by lower values (Dubovik et al., 2002). SSA values at 520 nm in Aarhus (this study) and Vavihill were very similar (0.85 ± 0.08 in Aarhus vs. 0.88 ± 0.05 in Vavihill) (Genberg, 2012; Roldin, 2012; Tørseth et al., 2012). The mean SSA value at Lamezia Terme using a wavelength of 637 nm during the same period was 0.78 (Donateo et al., 2020), which is slightly lower but within the variability of the values from this study (0.82 ± 0.10 at 660 nm).

The average value of $AAE_{470/660\,nm}$ throughout the campaign was 1.37 ± 0.26, which is well comparable to values reported for aerosols from fossil fuel combustion of 1 to 1.5 (Lee et al., 2012). The mean value of $SAE_{450/550\,nm}$ was 1.15 with a relatively large standard deviation of 0.74, indicating more variability in the wavelength dependence of the scattering coefficient. This variability can typically be explained by a change in the dominant aerosol particle mode as larger particles are described by smaller SAE values and vice versa. $SAE_{440/675\,nm}$ values for aerosols from fossil fuel combustion were previously reported larger than 1.2 (Bahadur et al., 2012) indicating smaller particles, while $SAE_{440/675\,nm}$ of dust and $SAE_{467\text{-}660\,nm}$ of sea salt were reported to be less than 0.5 (Bahadur et al., 2012; Costabile et al., 2013), indicating larger particles. This suggests that both fine and coarse mode particles occurred during this Aarhus Bay campaign, which is also in agreement with the mean value of ΔSAE of 0.22, suggesting the presence of both modes (Perrone et al., 2018; Suchánková et al., 2024). Few other studies exist reporting similar data for coastal environments: a monthly mean $AAE_{370/950\,nm}$ for April 2013 of approximately 1.3 was found in Vavihill (Sweden) (Martinsson et al., 2014), in-line with our data, while Donateo et al. (2020) reported a mean $SAE_{450/700\,nm}$ of 1.95 during the cold season (October to March from 2015 to 2018) in the coastal city Lamezia Terme (Italy). The substantially lower SAE value from this study indicates the presence of more large particles in Aarhus Bay compared to the Mediterranean coastal city.

The mean backscatter ratios, *b*, at 450 nm, 525 nm and 635 nm were 0.12, 0.13 and 0.14 with the same standard deviations of 0.02. As larger particles scatter predominately in the forward direction, such small *b* values support the SAE and ΔSAE results highlighting, the presence of in general larger particles. These values are in line with those found in Lamezia Terme

https://doi.org/10.5194/ar-2025-34
Preprint. Discussion started: 7 November 2025

during the cold season (October to March from 2015 to 2018) of 0.10, 0.11, 0.11 at 450 nm, 550 nm and 700 nm (Donateo et al., 2020), respectively. The mean values and standard deviations of the asymmetry parameter, g, in Aarhus were 0.60 ± 0.04, 0.59 ± 0.04, 0.58 ± 0.05 at 450 nm, 525 nm and 635 nm, respectively, which is comparable to those at similar wavelengths in Lamezia Terme during cold season, found to be 0.66 (450 nm), 0.63 (550 nm) and 0.65 (700 nm) (Donateo et al., 2020).

Figure 3 depicts time series of the total number concentration (N_{TOT}; Fig. 3(a)), number size distribution (dN/dlogDp; Fig. 3(b)), and surface area size distribution (dS/dlogDp; Fig. 3(c)) measured at Aarhus Bay. Both the total number concentration and size distributions are depicted as hourly averages. The size distributions are plotted for particles above 300 nm. The changes in N_{TOT} follow the same trend as was observed for σ_{sca} and σ_{abs}; i.e. the periods that were found to have high σ_{sca} and σ_{abs} have also high N_{TOT} as seen in Fig. 3(a). From 17 March to 20 March, the highest total particle number concentration was observed, with a maximum concentration of ∼550 # cm^{-3}. Elevated total particle number concentrations were also detected from 9 March to 11 March and from 29 March to 31 March. The average total particle number concentration throughout the whole period was 58.04 ± 70.15 # cm^{-3}. Number size distributions highlight particles between the detection limit of the WELAS and approximately 1 µm and surface size distributions more clearly depict the contribution of particles up to 7 µm. When comparing the evolution of N_{TOT} with the number and surface size distributions (Fig. 3(b) and 3(c)), it is evident that the period with the highest particle number concentration coincided with the number and surface size distributions dominated by smaller particle sizes, indicating an enhanced abundance of small particles during this period. Generally, when the number and surface size distributions show a mode above 0.5 µm in particle diameter, the total number concentration remained below 200 # cm^{-3} and was typically less than 100 # cm^{-3}.

3.2 Daily patterns of scattering and absorption coefficient and eBC

Figure 4 illustrates the median diurnal variation of σ_{sca}, σ_{abs} and eBC concentrations during weekdays (4(a), 4(c), and 4(e)) and weekends (4(b), 4(d), and 4(f)). Median values were calculated excluding the data from 17 to 19 March, which showed the highest concentrations. Except for σ_{sca} during weekdays, σ_{abs} and σ_{sca} show similar trends, with two major peaks, one in the morning and one during the evening/night, highlighting the typical rush hours. The morning peak is generally around 5-9 h, while the evening peak typically lasts from 17-23 h.

The scattering signal did not show a clear pattern during weekdays, however, two distinct peaks could be observed during the weekend (Fig. 4(a) and 4(b)). Furthermore, the difference between the three wavelengths was larger on weekdays than on weekends. During weekends, σ_{sca} values were very close to each other between 10 and 18 h, indicating that both smaller and larger particles were present, while the signal at 450 nm was clearly higher during weekdays in the same time period, indicating a larger fraction of small particles. The absorption signal in the morning appeared earlier and sharper during weekdays than during weekends, coinciding with expected traffic patterns during weekdays and weekends, respectively. The evening peak was slightly lower during weekdays than during weekends (Fig. 4(c) and 4(d)). Figures S3(a) and S3(b) show the temporal evolution of the diurnal patterns of scattering and absorption coefficients, highlighting that except for the last week, the daily patterns were quite comparable throughout the course of the campaign.

https://doi.org/10.5194/ar-2025-34
Preprint. Discussion started: 7 November 2025

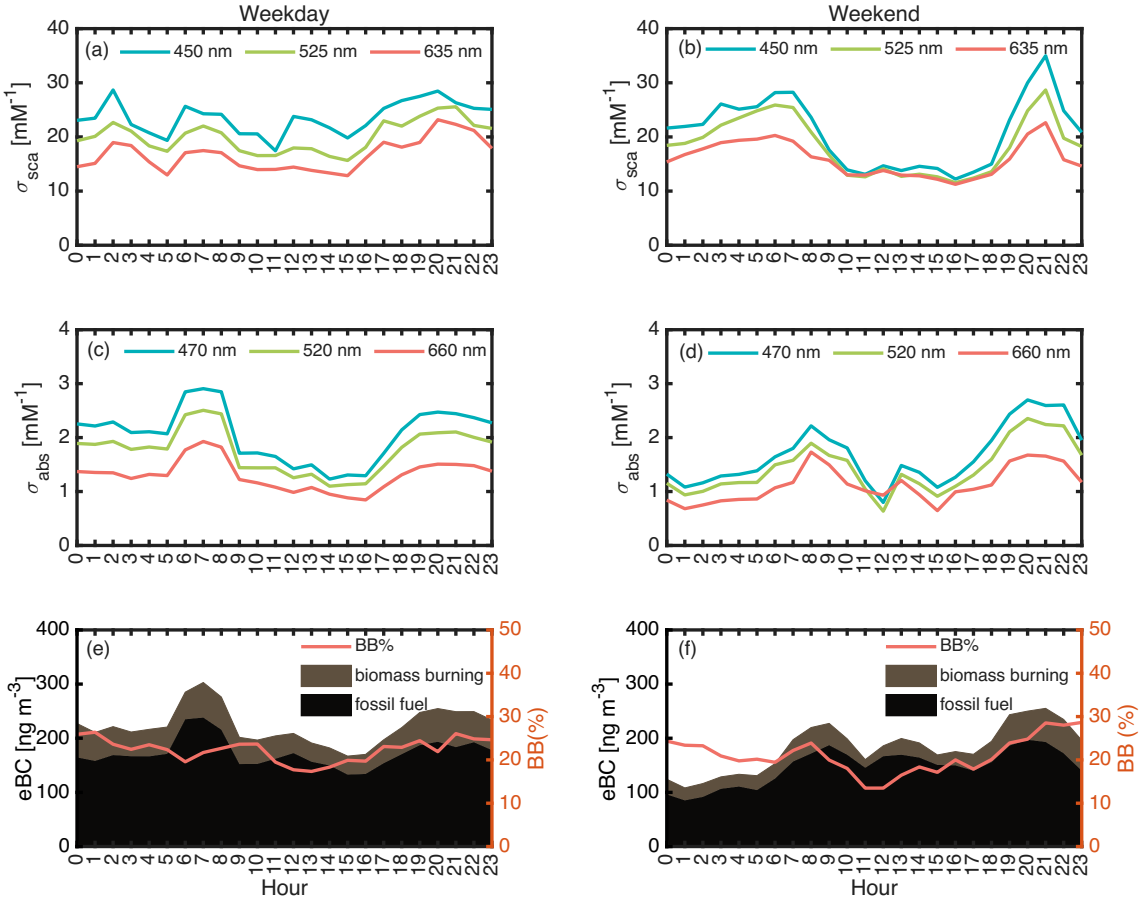

Figure 4. Diurnal variation of (a) median σ_{sca} values at three wavelengths during weekdays, (b) σ_{sca} at three wavelengths during weekends, (c) median values of σ_{abs} at three wavelengths during weekdays, (d) median values of σ_{abs} at three wavelengths during weekends, (e) median values of eBC during weekdays, (f) median values of eBC during weekends. In (e) and (f), brown colours represent contribution from biomass burning and black colours from fossil fuels. Source apportionment is based on BB%, see text for more information.

https://doi.org/10.5194/ar-2025-34
Preprint. Discussion started: 7 November 2025

The contribution from combustion of fossil fuels was calculated by subtracting the contribution from biomass burning from the total eBC. Figure 4(e) and 4(f) present eBC values subdivided in fossil fuel (black) and biomass burning (brown) contributions. Fossil fuel contributed the most to eBC concentrations, above 70 % during both weekdays and weekends. BB% varied from 17 % to 26 % during weekdays, and from 13 % to 29 % during weekends. During weekdays, a prominent peak during rush hour was observed from around 5 to 8 h, underlining the important influence of traffic emissions at the site. In particular, the increase on weekdays was larger than that on weekends. During the evening, an increase in both fossil fuel and biomass burning contributions was found on weekends and weekdays. Notably, the contribution from biomass burning was higher during weekend, where it increased from 20 % to 29 % between 18 and 23 h. This could arise from the increased use of domestic fireplaces during weekend and bonfires.

In addition to human activities such as traffic and biomass burning, changes in the planetary boundary layer (PBL) height may impact daily patterns. A high PBL typically leads to dilution of surface emissions and in general lower concentrations, while a lower PBL leads to up-concentrations of emissions. Solar radiation is the major driver for PBL height and can be used as a proxy. Figure S4 shows the overall radiation time per day and Fig. S5 illustrates the diurnal variation of solar radiation during the campaign. The typical radiation pattern showed an increase from around 7 to 8 h and a decrease around 19 to 21 h, where the decrease shifts to later hours at the end of the campaign. This coincides well with the time the morning peaks start to decrease and the time the evening peaks start to increase.

3.3 Comparison between measured and modelled black carbon

Figure 5 highlights a very good agreement between the temporal evolution of total eBC, as measured by the aethalometer, and BC, as modelled by FLEXPART analysis. FLEXPART separates the contribution from black carbon into eight different sources (see Fig. S6 for the time series of the individual sources). On average, the main BC sources contributing to the air masses in Aarhus Bay during the campaign were DOM ($\sim$ 49 %), BB ($\sim$ 26 %), TRA ($\sim$ 19 %) and IND ($\sim$ 3 %), while minor contributions from FLR ($\sim$ 2 %), SHP and WSD ($\sim$ 1 %) and ENE ($\sim$ 0 %) were found. Overall modelled values underestimated the BC mass concentrations by $\sim$ 60 %.

3.4 Characterization of three special air mass types

We selected three special cases from the entire measurement period that were characterized by different air mass types:

1. Case 1: "Local pollution": This period lasted 48 hours, from 17 March 18:10 to 19 March 18:20. It was characterized by high scattering and absorption coefficients, reaching the highest values during the campaign. The measured wind speed (2.23 ± 1.72 m s^{-1}) and radiation were relatively low during this period, as recorded at the DMI station, providing favourable conditions for particle accumulation.

2. Case 2: "High Single Scattering Albedo": This period lasted 52 hours, from 23 March 10:40 to 25 March 14:40. During this period, highest SSA values were reached, as well as higher wind speeds (5.42 ± 1.87 m s^{-1}), with a maximum of 10.2 m s^{-1} (from DMI station). This combination could favour a marine emission source.

https://doi.org/10.5194/ar-2025-34
Preprint. Discussion started: 7 November 2025

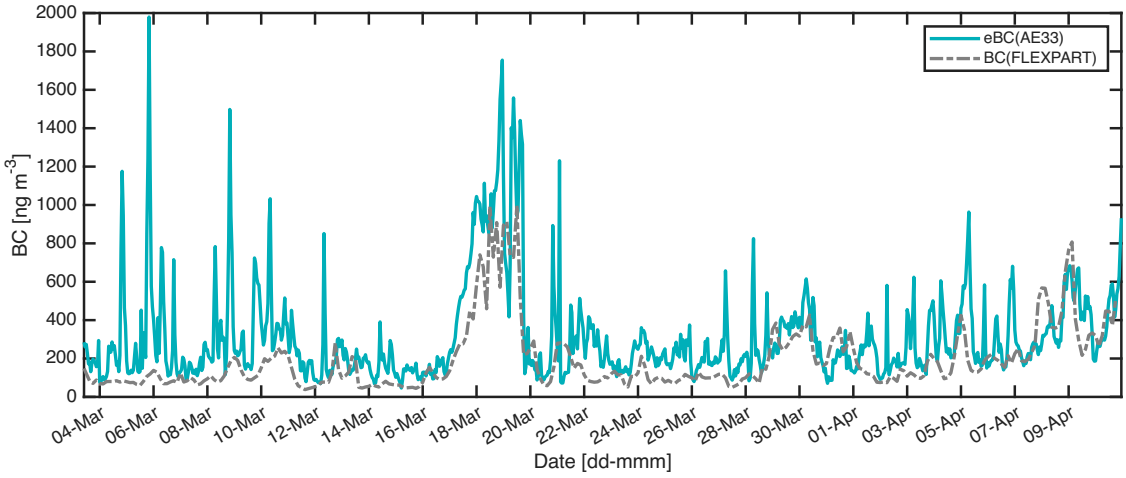

Figure 5. Black carbon mass concentrations measured by the aethalometer (blue solid line) and modelled using FLEXPART (grey stippled line) combining the all source contributions.

3. Case 3: "Long-range transport": This case lasted 48 hours, from 7 April 3:00 to 9 April 3:00. Based on the results of the FLEXPART model, significant contributions to BC originated from the "Asia" and "Russia" sectors. Wind speed was low with a mean value of 2.65 ± 1.66 m s^{-1} and the wind direction mainly originated from Northeast and East-Northeast (from DMI station), in agreement with the FLEXPART results.

Figure S7 presents footprint analysis for each of the selected cases while Fig. S8 shows CO, PM_{10}, and NO_x data from DCE station, highlighting the case periods. Figure S9 shows time series of wind speed and wind direction during the entire measurement period.

3.4.1 Case 1:

Both σ_{sca} and σ_{abs} were around three to four times higher than the mean of the entire measurement period, as seen in Table 1. Also, the total number concentration was 225.53 ± 111.43 # cm^{-3} and thus almost four times higher than the mean value during the whole period. NO_x and CO are often used as tracers of pollution as they are mainly emitted from fossil fuel combustion and CO may also originate from biomass burning. NO_x has a short lifetime of around one day and a limited travel range usually below one km Seinfeld and Pandis (2016) and is thus indicative of local emissions. CO, on the other hand, has a lifetime of below 1 year and a travel range of about 50 km Seinfeld and Pandis (2016), thus representing more regional air masses. NO_x concentrations varied from approximately 15 to 109 ppb with an average value of 49 ppb and a standard deviation of 23 ppb (Fig. S10). This is 160 % higher than the mean NO_x mixing ratios (17.96 ± 17.31 ppb) measured during the entire measurement period at that location. Meanwhile, the mean CO concentration during Case 1 was 0.29 ± 0.09 ppm, ranging from 0.16 ppm to 0.59 ppm. This is 55 % higher than the mean value over the whole measurement period of 0.18 ± 0.05 ppm. Thus, both the

https://doi.org/10.5194/ar-2025-34
Preprint. Discussion started: 7 November 2025

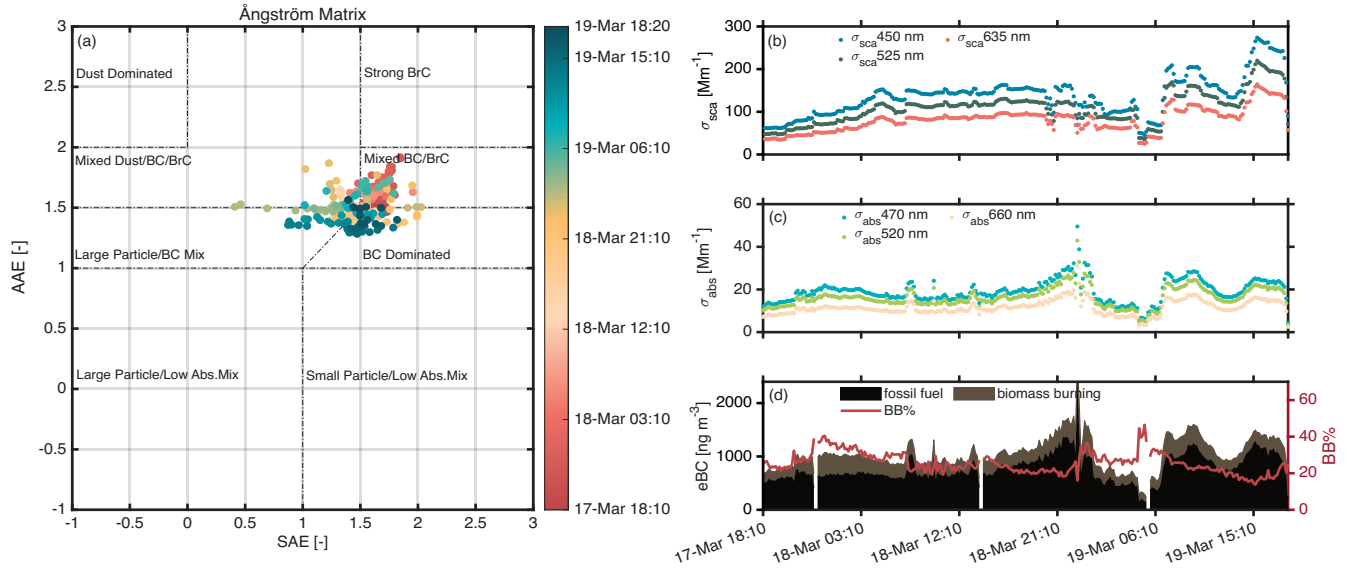

Figure 6. Optical properties and eBC concentration during Case 1. (a) Ångström matrix colour-coded by time; (b) time series of scattering coefficients; (c) time series of absorption coefficients; (d) source apportionment of eBC based on the biomass burning percentage (BB%) provided by the aethalometer.

elevated levels of NO_x and CO indicate that Case 1 was dominated by local emissions most probably originating from ships or local traffic. FLEXPART footprint analysis for Case 1 revealed a clear continental contribution (see Fig. S7) and an age of 3 days for on average 76 % of BC data, where 91 % of BC originated from Europe (see Fig. S11), suggesting that the aerosols were rather fresh and probably emitted from local sources.

As illustrated in Fig.6(a), most data points were concentrated in the "BC-dominated" and "mixed BC/BrC" zones. The average values of $AAE_{532/660\ nm}$ and $SAE_{450/550\ nm}$ were 1.52 and 1.49, respectively. Figure 6(d) shows that the contribution of fossil fuel combustion to eBC was significant during this period. Aerosols from fossil fuel combustion represented 75.03 % of the eBC concentration, ranging from 52.51 % to 86.31 %, which was slightly higher than during the entire measurement period. Figures 6(b) and (c) present the temporal evolution of σ_{sca} and σ_{abs} during Case 1. It is evident that σ_{sca} increased slightly until 18 March 5:00, while σ_{abs} first increased but then stopped increasing earlier on 17 March 23:00 and subsequently decreased until 18 March 5:00. During this period, aerosols gathered in the "mixed BC/BrC" range as biomass burning had a significant impact on eBC during this time (d). After 18 March 5:00, both σ_{sca} and σ_{abs} remained at a constant level until 18 March 20:00. From 18 March 20:00 to midnight of 19 March, σ_{sca} and σ_{abs} show different trends: while σ_{sca} shows two dips, σ_{abs}, on the contrary, increased to reach the highest values. During the σ_{abs} peak, the data points were gathered in the "BC dominated" zone (a) and a clear signal from fossil fuels is visible in the source distribution plot (d). After midnight on 19 March, both scattering and absorption coefficients started to decrease, possibly due to a change in the meteorology, as all data recorded at the DCE station decreased simultaneously with the optical signals as seen in Fig. S10. At the end of Case 1, both

https://doi.org/10.5194/ar-2025-34
Preprint. Discussion started: 7 November 2025

AEROSOL Research Discussions

σ_{sca} and σ_{abs} increased again and then stabilized. Notably, σ_{sca} reached the highest values during this end phase of Case 1. Here, particles were gathered in the "large particle/BC Mix" zone and moved towards the "BC dominated" zone (a). Figure 6 (d), illustrates that BB% continuously decreased during this period, while traffic emissions dominated the signal.

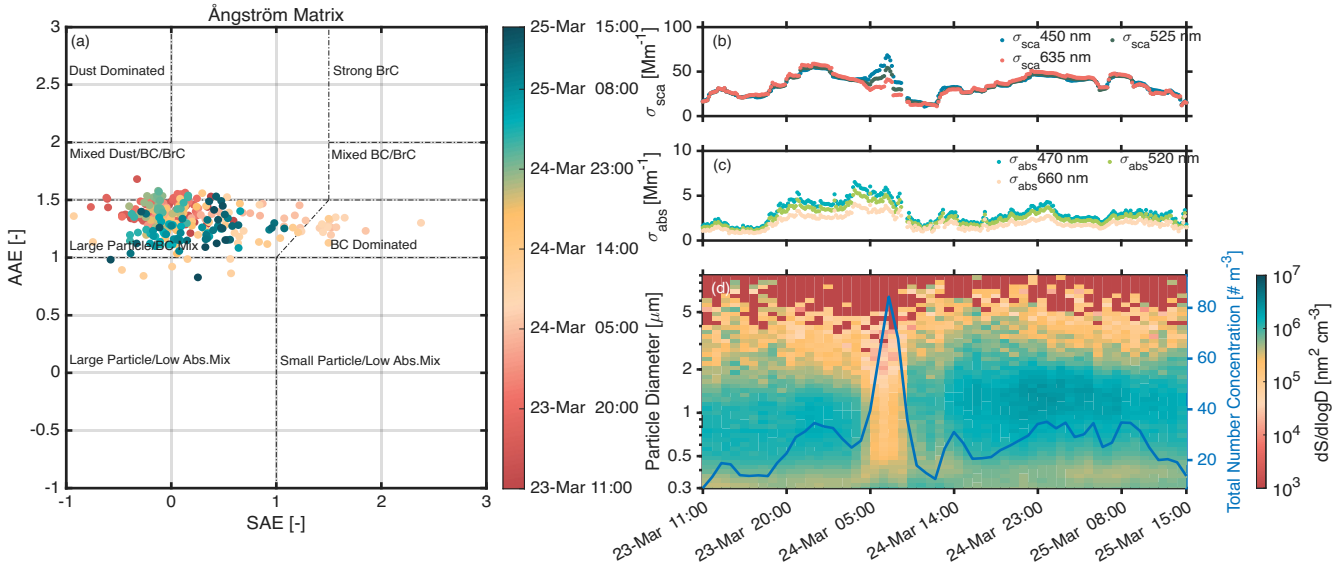

Figure 7. Optical and physical properties during Case 2. (a) Ångström matrix colour-coded by time; (b) time series scattering coefficients; (c) time series of absorption coefficients; (d) time evolution of surface area size distribution and total number concentration.

3.4.2 Case 2:

During Case 2, the highest SSA values during the whole campaign with a mean value of 0.93 at 520 nm were recorded, indicating that highly scattering particles constituted a significant portion of the aerosols throughout this period. As shown in Table1, the mean scattering coefficients were higher in Case 2 (34.62 $\pm$ 10.91 Mm^{-1} at 525 nm) than during the entire period (29.02 $\pm$ 27.39 Mm^{-1} at 525 nm). Conversely, the absorption coefficients were lower during Case 2 (2.64 $\pm$ 1.03 Mm^{-1} at 520 nm) than during the whole measurement period (4.53 $\pm$ 4.43 Mm^{-1} at 520 nm). Consequently, the SSA values were comparatively high in relation to the values during the entire period (0.93 $\pm$ 0.02 at 520 nm).

The AAE values during Case 2 (1.32 $\pm$ 0.14) were slightly lower than the mean of the entire period (1.41 $\pm$ 0.28). The average SAE values during Case 2 (0.17 $\pm$ 0.52) were significantly lower than the average values for the entire period (1.15 $\pm$ 0.74), suggesting that large particles dominated the overall aerosol population. Thus, in the Ångström matrix (Fig.7(a)), the data are clustered together in the "Large particle / BC mixture" zone. Only during midnight on 24 March (orange points), data points were shifted to the "BC dominated" zone before shifting back to the "Large particle/ Low Abs mix" zone.

Figure 7(b) shows that, during this shift, σ_{sca} at different wavelengths was clearly different, while the signal mostly overlapped during the rest of Case 2, leading to low SAE values that are typical for large particles. The absorption coefficients

https://doi.org/10.5194/ar-2025-34
Preprint. Discussion started: 7 November 2025

(c) generally followed the trend of scattering, except for the special short period observed on 24 March, which lasted approximately 3 hours. Figure 7(d) highlights that in terms of surface area, particles of 0.35 to 5 µm in diameter dominated, with a mode diameter around 1 µm. Clarke et al. (2003) reported that breaking waves produce aerosols in all sizes from 10 nm to greater than 10 µm. Additionally, the size distributions clearly point out that during the special period on 24 March, the particle number concentration strongly increased to approximately 75 # cm^{-3} and sizes below 0.3 µm dominated, when "BC dominated" emissions were detected. The higher wind speeds recorded during Case 2, together with the low SAE values and measured larger particle sizes suggest a marine influence. The values that suddenly appeared in the "BC dominated" zone could have been due to ship or local traffic emissions. FLEXPART footprint analysis for Case 2 revealed a contribution from air masses arriving from the ocean (see Fig. S7), thus supporting an impact by marine particles.

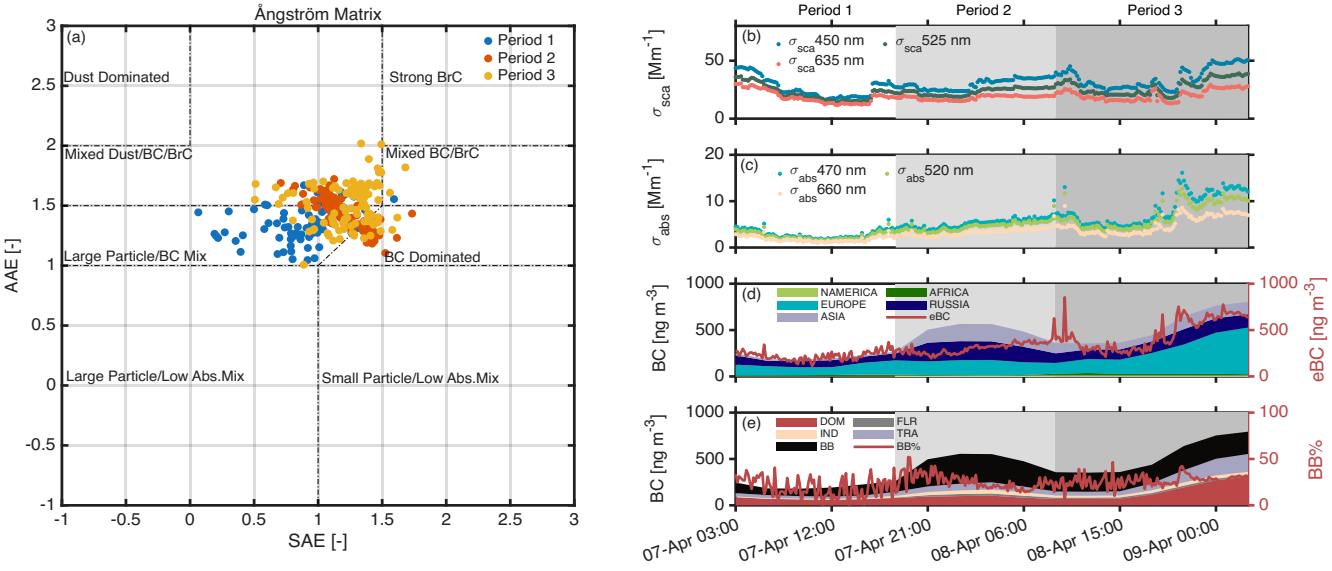

Figure 8. Optical properties and FLEXPART results during Case 3. (a) Ångström matrix colour-coded by time; (b) time series of scattering coefficients; (c) time series of absorption coefficients; (d) continental contribution to the BC concentration from FLEXPART and eBC from aethalometer; (e) source contributions of BC from FLEXPART (DOM: residential and commercial combustion, FLR: gas flaring, SHP: shipping activities, TRA: surface transportation, ENE: power plants and energy conversion, IND: industrial combustion, WST: waste burning, BB: biomass burning.) and BB% from aethalometer shown with the red line.

3.4.3 Case 3:

According to the FLEXPART model results, Russia and Asia contributed significantly to the BC concentrations during Case 3, leading to a more "long-range" dominated aerosol. This is also clearly visible in the FLEXPART footprint analysis for Case 3 (see Fig. S7).

https://doi.org/10.5194/ar-2025-34
Preprint. Discussion started: 7 November 2025

AEROSOL Research Discussions

Figure 8 shows the measured optical properties and source apportionment, and continental contributions of BC from the FLEXPART model results. Based on Fig. 8(d), Case 3 was subdivided into three periods: PERIOD 1: From 3:00 to 19:00 on 7 April, with a contribution from Russia of around 34 %, 50 % from Europe and 8 % from Asia. PERIOD 2: From 19:00 on 7 April to 9:00 on 8 April, with increased contributions from Asia and Russia, reaching around 27 % and 34 %, respectively, while contributions from Europe were 34 %. PERIOD 3: From 9:00 on 8 April to 3:00 on 9 April, with contributions from Asia and Russia remaining constant (approximately 20 % and 26 %) while the contribution from Europe increased over time to reach 48 %.

Figure 8(a) shows the Ångström matrix, which is colour-coded by the 3 periods introduced above. The points are initially located in the "Large Particle/BC Mix" zone (PERIOD 1), then shift to the "Mixed Dust/BC/BrC" and "BC Dominated" zones (PERIOD 2), and finally spread between the "Mixed Dust/BC/BrC", "BC Dominated", "Mixed BC/BrC" and "Large Particle /BC Mix" zones during PERIOD 3. This indicates that PERIOD 1 contained a high fraction of large particles, then the average particle size decreased while the BC fraction increased during PERIOD 2. During PERIOD 3, the BC and BrC fractions increased while SAE values increased, highlighting smaller particles.

Figure 8(b) illustrates the scattering and (c) absorption coefficients at different wavelengths over time. During PERIOD 1, the scattering coefficient at 525 nm decreased from 40 to 10 Mm^{-1}, and the absorption coefficient at 525 nm decreased from 4 to 2 Mm^{-1}. The average SSA value was 0.90. The similar σ_{sca} values at the three wavelengths, lead to the observed clustering in the "Large Particle/BC Mix" zone (Fig. 8(a)). During PERIOD 2, the scattering and absorption coefficients began to increase. The SSA dropped to 0.84, indicating an increase in the contribution by absorbing aerosols. During PERIOD 3, the scattering and absorption coefficients first briefly decreased and subsequently increased again, fluctuating but both following similar trends, while SSA values decreased to 0.80.

Figure 8(d) highlights that the temporal evolution of BC concentration from FLEXPART and eBC concentration aethalometer measurements agreed well during case 3. Only during PERIOD 2 the modelled BC concentrations appeared higher than the measured eBC concentrations. The mean BC concentration obtained from the FLEXPART model during Case 3 was 423.6 ng m^{-3}, while the aethalometer's mean eBC concentration during Case 3 was 376.2 ng m^{-3}. Figure 8(e) divided BC into different emission sources. According to FLEXPART, biomass burning (BB) significantly contributed to PERIODS 1-3, especially PERIOD 2. BC concentrations from BB reached highest values with increasing contributions from Asia and Russia, while transport (TRA) and domestic (DOM) emissions increased during PERIOD 3 simultaneously with an increasing contribution from Europe (Fig. 8(d)). The mean BB% from the aethalometer was approximately 24 $\pm$ 9 % during the whole case study and its evolution during PERIODS 1-3 appeared rather constant, not following the FLEXPART BB signal, which is 48$\pm$ 9 %. On the other hand, the evolution of the eBC concentration is well comparable with the signal from the domestic sector. A discrepancy between BB% and FLEXPARTs' BB concentration could potentially arise from the fact that while FLEXPART clearly separates between BB and DOM, the signal might be mixed in the aethalometer measurement.

The mean NO_x mixing ratio measured at the DCE station during this case, was 13.30 $\pm$ 8.46 ppb, which was lower than the whole campaign period average of 17.96 $\pm$ 17.31 ppb. Similarly, the mean CO concentration was 0.16 $\pm$ 0.03 ppm and thus comparable to the mean value of the whole period (0.18 $\pm$ 0.055 ppm). Figure S15 shows that NO_x decreased sharply below

https://doi.org/10.5194/ar-2025-34
Preprint. Discussion started: 7 November 2025

5 ppm around 00:00 on 8 April (PERIOD 2), and then increased again. However, the eBC concentration continually increased while the NO_x concentration decreased. This suggests that the BC was likely transported from other regions, as FLEXPART suggested, such as Asia and Russia, instead of being emitted locally. During PERIOD 3, the NO_x and eBC concentrations increased drastically, indicating that the pollutants were derived from local emissions. This is consistent with the BC results from the FLEXPART model and the increased contribution from Europe during this period.

4 Conclusions

Aerosol properties were investigated during five weeks from March to mid April 2023 at the coastal site - Aarhus Bay, Denmark. Aerosol absorption and scattering coefficients as well as size distributions were continuously monitored to investigate the aerosol type and infer the main aerosol sources during the selected period. Specifically, the study aimed to assess the importance of anthropogenic vs. natural, including marine, sources at this coastal area. Additionally, a comparison to footprint, airmass source and age analysis from the FLEXPART model was carried out.

Scattering and absorption coefficients were relatively low during the whole period (σ_{sca} = 29.02 ± 27.39 Mm^{-1}, σ_{abs} = 4.53 ± 4.43 Mm^{-1} at λ = 525 nm), similar to what was found in other Scandinavian locations (Genberg, 2012; Roldin, 2012; Tørseth et al., 2012) and lower compared to Mediterranean coastal cities (Donateo et al., 2020). SSA varied from 0.28 to 0.9, pointing to both, periods with high absorbing, most likely anthropogenic, and highly scattering, potentially marine, influences. The wavelength dependence of absorption, highlighted a substantial impact from biomass burning aerosols of on average 22.90 ± 11.93 %. This can be attributed to emissions from domestic fireplaces which are common in the Aarhus area (Plejdrup et al., 2021). The wavelength dependence of scattering coefficient showed large variability due to changes in the particle size distribution. This was corroborated by the recorded size spectra showing periods with high number concentrations and mostly, small sizes and several periods with lower number concentrations and particle diameters above 1 µm. Compared to a Mediterranean coastal city during a similar period, particles in Aarhus appeared on average larger (Donateo et al., 2020). Daily patterns in Aarhus Bay revealed a diurnal variation related to traffic and biomass burning emissions detected in the absorption coefficients, both during weekdays and weekends. Interestingly, scattering coefficients revealed a pattern only during weekends, with highest scattering coefficients during the evening hours between 18 and 23 h.

Wavelength dependences in scattering and absorption were explored by the Ångström matrix and combined with FLEXPART analysis to pinpoint major aerosol sources in Aarhus Bay. Periods with local anthropogenic pollution, highly scattering aerosols, and particles from long-range transport were observed. Using the Ångström classification scheme proposed by (Cappa et al., 2016), aerosols during the whole campaign were to 48 % characterized by 'BC dominated', 31 % by 'Large Particles/BC mix', 7.7 % by 'Large Particles/Low Abs. Mix', 4.3 % by 'Small Particles/Low Abs. Mix', 4.2 % by 'Mixed Dust/BC/BrC', 4.1 % by 'Mixed BC/BrC' and 0.85 % by 'Strong BrC' (see Fig. S17). According to FLEXPART the average continental contribution to BC concentrations was ∼ 71 % from Europe, ∼ 10 % from Russia, ∼ 9 % Asia, ∼ 6 % North America, ∼ 2 % Africa, ∼ 1 % Central America and the Ocean. Besides, the air mass age as modelled by FLEXPART underscores the mixture of both freshly emitted and several week-old air masses present in the Aarhus Bay area (see Fig. S18).

https://doi.org/10.5194/ar-2025-34
Preprint. Discussion started: 7 November 2025

In particular, three distinct cases were chosen to describe typical aerosol properties in Aarhus Bay. "Case 1" describes a typical local pollution event, characterized by highest scattering and absorption coefficients and simultaneously strongly elevated NO_x and CO mixing ratios. According to the Ångström matrix, most data could be described as 'BC-dominated' and 'mixed BC/BrC', with on average 75 % originating from fossil fuel combustion. Particle number concentrations reached highest values but contained predominately particle sizes below 500 nm. eBC data compared well with modelled values from FLEXPART highlighting the large contribution from fossil fuels. FLEXPART analysis showed a clear influence by continental air masses. "Case 2" highlights the period with the highest SSA values during the measurement campaign. Both SAE and size distribution measurements indicate the presence of large particles that are mainly described by the 'Large Particles/BC mix' area in the Ångström matrix. The higher wind speeds during the "Case 2" period and lower absorption coefficients, could indicate a larger contribution by marine particles during this period, which is also suggested by FLEXPART footprint analysis. "Case 3" denotes an event with air masses from long-range transport. FLEXPART analysis yielded a larger contribution by the sectors "Russia" and "Asia" impacting BC concentrations particularly at the beginning of "Case 3", which were characterized by smaller particles, as evidenced by smaller SAE values, compared to local events dominated by the "Europe" sector.

Data availability. Data will be available on Zenodo.

Author contributions. B.R. designed and supervised the research; Z.T., J.S.T. and B.R. conducted field experiments; Z.T. analysed the scattering and absorption measurements, J.T.S. analysed the spectrometer measurements and performed loss calculations; N.E. and S.E. performed FLEXPART simulations; B.R., A.M., H.S. and M.B. contributed to interpreting the results. Z.T., J.T.S. and B.R. wrote the paper with contributions from all co-authors. All authors read and reviewed the manuscript.

Competing interests. The authors declare no conflict of interest.

Acknowledgements. This work was supported by a research grant from Villum Fonden (42128), and the aethalometer (AE33, Aerosol Magee Scientific) was loaned from Villum Research Station. We would like to thank Peter Ravn and Torben Sigsgaard for their support for offline measurements and Henrik Birkedal for loaning the microscope. We acknowledge the support of the Center of Excellence for Chemistry of Clouds (C3), funded by the Danish National Research Foundation (DNRF172). FLEXPART simulations are cross-atmospheric research infrastructure services provided by ATMO-ACCESS (EU grant agreement No 101008004). The computations/simulations were performed on resources provided by Sigma2 - the National Infrastructure for High Performance Computing and Data Storage in Norway. We acknowledge the Danish Ministry of Environment and Department of Environmental Science at Aarhus University, for collecting and providing NO_x and CO data and support for this study. And we acknowledge the Danish Meteorological Institute providing Meteorology data.

https://doi.org/10.5194/ar-2025-34
Preprint. Discussion started: 7 November 2025

AEROSOL Research Discussions

References

Ahlberg, E., Ausmeel, S., Nilsson, L., Spanne, M., Pauraite, J., Klenø Nøjgaard, J., Bertò, M., Skov, H., Roldin, P., Kristensson, A., et al.: Measurement report: Black carbon properties and concentrations in southern Sweden urban and rural air–the importance of long-range transport, Atmospheric Chemistry and Physics, 23, 3051–3064, https://doi.org/10.5194/acp-23-3051-2023, 2023.

Andrews, E., Sheridan, P. J., Fiebig, M., McComiskey, A., Ogren, J. A., Arnott, P., Covert, D., Elleman, R., Gasparini, R., Collins, D., Jonsson, H., Schmid, B., and Wang, J.: Comparison of methods for deriving aerosol asymmetry parameter, Journal of Geophysical Research: Atmospheres, 111, https://doi.org/10.1029/2004JD005734, 2006.

Bahadur, R., Praveen, P. S., Xu, Y., and Ramanathan, V.: Solar absorption by elemental and brown carbon determined from spectral observations, Proceedings of the National Academy of Sciences, 109, 17 366–17 371, https://doi.org/10.1073/pnas.1205910109, 2012.

Barman, N., Kundu, S. S., and Borgohain, A.: Observation and model simulation of aerosol optical properties and size distribution over the hilly terrain of Northeast India, Aerosol Science and Engineering, 8, 319–335, https://doi.org/10.1007/s41810-024-00225-9, 2024.

Bellouin, N., Boucher, O., Haywood, J., and Reddy, M. S.: Global estimate of aerosol direct radiative forcing from satellite measurements, Nature, 438, 1138–1141, https://doi.org/10.1038/nature04348, 2005.

Bergstrom, R. W., Russell, P. B., and Hignett, P.: Wavelength Dependence of the Absorption of Black Carbon Particles: Predictions and Results from the TARFOX Experiment and Implications for the Aerosol Single Scattering Albedo, AMS, Journal of the Atmospheric Sciences, https://doi.org/10.1175/1520-0469(2002)059<0567:WDOTAO>2.0.CO;2, 2002.

Bohren, C. F. and Huffman, D. R.: Absorption and scattering of light by small particles, John Wiley & Sons, 2008.

Bond, T. C. and Bergstrom, R. W.: Light Absorption by Carbonaceous Particles: An Investigative Review, Aerosol Science and Technology, 40, 27–67, https://doi.org/10.1080/02786820500421521, 2006.

Bond, T. C., Doherty, S. J., Fahey, D. W., Forster, P. M., Berntsen, T., DeAngelo, B. J., Flanner, M. G., Ghan, S., Kärcher, B., Koch, D., Kinne, S., Kondo, Y., Quinn, P. K., Sarofim, M. C., Schultz, M. G., Schulz, M., Venkataraman, C., Zhang, H., Zhang, S., Bellouin, N., Guttikunda, S. K., Hopke, P. K., Jacobson, M. Z., Kaiser, J. W., Klimont, Z., Lohmann, U., Schwarz, J. P., Shindell, D., Storelvmo, T., Warren, S. G., and Zender, C. S.: Bounding the role of black carbon in the climate system: A scientific assessment, Journal of Geophysical Research: Atmospheres, 118, 5380–5552, https://doi.org/10.1002/jgrd.50171, 2013.

Böttcher, K., Paunu, V.-V., Kupiainen, K., Zhizhin, M., Matveev, A., Savolahti, M., Klimont, Z., Väätäinen, S., Lamberg, H., and Karvosenoja, N.: Black carbon emissions from flaring in Russia in the period 2012–2017, Atmospheric Environment, 254, 118 390, https://doi.org/10.1016/j.atmosenv.2021.118390, 2021.

Cappa, C. D., Kolesar, K. R., Zhang, X., Atkinson, D. B., Pekour, M. S., Zaveri, R. A., Zelenyuk, A., and Zhang, Q.: Understanding the optical properties of ambient sub-and supermicron particulate matter: results from the CARES 2010 field study in northern California, Atmospheric Chemistry and Physics, 16, 6511–6535, https://doi.org/10.5194/acp-16-6511-2016, 2016.

Cassiani, M., Stohl, A., and Brioude, J.: Lagrangian stochastic modelling of dispersion in the convective boundary layer with skewed turbulence conditions and a vertical density gradient: Formulation and implementation in the FLEXPART model, Boundary-Layer Meteorology, 154, 367–390, https://doi.org/10.1007/s10546-014-9976-5, 2015.

Cazorla, A., Bahadur, R., Suski, K. J., Cahill, J. F., Chand, D., Schmid, B., Ramanathan, V., and Prather, K. A.: Relating Aerosol Absorption Due to Soot, Organic Carbon, and Dust to Emission Sources Determined from in-Situ Chemical Measurements, Atmospheric Chemistry and Physics, 13, 9337–9350, https://doi.org/10.5194/acp-13-9337-2013, 2013.

https://doi.org/10.5194/ar-2025-34
Preprint. Discussion started: 7 November 2025

Clarke, A., Kapustin, V., Howell, S., Moore, K., Lienert, B., Masonis, S., Anderson, T., and Covert, D.: Sea-salt size distributions from breaking waves: Implications for marine aerosol production and optical extinction measurements during SEAS, Journal of Atmospheric and Oceanic Technology, 20, 1362–1374, https://doi.org/10.1175/1520-0426(2003)020<1362:SSDFBW>2.0.CO;2, 2003.

Cosby, A., Lebakula, V., Smith, C., Wanik, D., Bergene, K., Rose, A., Swanson, D., and Bloom, D.: Accelerating growth of human coastal populations at the global and continent levels: 2000–2018, Scientific Reports, 14, https://doi.org/10.1038/s41598-024-73287-x, 2024.

Costabile, F., Barnaba, F., Angelini, F., and Gobbi, G.: Identification of key aerosol populations through their size and composition resolved spectral scattering and absorption, Atmospheric Chemistry and Physics, 13, 2455–2470, https://doi.org/10.5194/acp-13-2455-2013, 2013.

Dall'Osto, M., Ceburnis, D., Martucci, G., Bialek, J., Dupuy, R., Jennings, S., Berresheim, H., Wenger, J., Healy, R., Facchini, M., et al.: Aerosol properties associated with air masses arriving into the North East Atlantic during the 2008 Mace Head EUCAARI intensive observing period: an overview, Atmospheric Chemistry and Physics, 10, 8413–8435, https://doi.org/10.5194/acp-10-8549-2010, 2010.

Donateo, A., Feudo, T. L., Marinoni, A., Calidonna, C. R., Contini, D., and Bonasoni, P.: Long-term observations of aerosol optical properties at three GAW regional sites in the Central Mediterranean, Atmospheric Research, 241, 104 976, https://doi.org/10.1016/j.atmosres.2020.104976, 2020.

Drinovec, L., Močnik, G., Zotter, P., Prévôt, A. S. H., Ruckstuhl, C., Coz, E., Rupakheti, M., Sciare, J., Müller, T., Wiedensohler, A., and Hansen, A. D. A.: The "dual-spot" Aethalometer: an improved measurement of aerosol black carbon with real-time loading compensation, Atmospheric Measurement Techniques, 8, 1965–1979, https://doi.org/10.5194/amt-8-1965-2015, 2015.

Dubovik, O., Holben, B., Eck, T. F., Smirnov, A., Kaufman, Y. J., King, M. D., Tanré, D., and Slutsker, I.: Variability of absorption and optical properties of key aerosol types observed in worldwide locations, Journal of the atmospheric sciences, 59, 590–608, https://doi.org/10.1175/1520-0469(2002)059<0590:VOAAOP>2.0.CO;2, 2002.

Fomba, K. W., Müller, K., van Pinxteren, D., Poulain, L., van Pinxteren, M., and Herrmann, H.: Long-term chemical characterization of tropical and marine aerosols at the Cape Verde Atmospheric Observatory (CVAO) from 2007 to 2011, Atmospheric Chemistry and Physics, 14, 8883–8904, https://doi.org/10.5194/acp-14-8883-2014, 2014.

Forster, C., Stohl, A., and Seibert, P.: Parameterization of Convective Transport in a Lagrangian Particle Dispersion Model and Its Evaluation, Journal of Applied Meteorology and Climatology, 46, 403 – 422, https://doi.org/10.1175/JAM2470.1, 2007.

Genberg, J.: ACTRIS, EMEP, GAW-WDCA, 2012, Aerosol absorption coefficient at Vavihill, data hosted by EBAS at NILU, https://doi.org/10.48597/7M2A-YGDC, 2012.

Grythe, H., Kristiansen, N. I., Groot Zwaaftink, C. D., Eckhardt, S., Ström, J., Tunved, P., Krejci, R., and Stohl, A.: A new aerosol wet removal scheme for the Lagrangian particle model FLEXPART v10, Geoscientific Model Development, 10, 1447–1466, https://doi.org/10.5194/gmd-10-1447-2017, 2017.

Hansen, A. D., Rosen, H., and Novakov, T.: The aethalometer—an instrument for the real-time measurement of optical absorption by aerosol particles, Science of the Total Environment, 36, 191–196, https://doi.org/10.1016/0048-9697(84)90265-1, 1984.

Hersbach, H., Bell, B., Berrisford, P., Hirahara, S., Horányi, A., Muñoz-Sabater, J., Nicolas, J., Peubey, C., Radu, R., Schepers, D., Simmons, A., Soci, C., Abdalla, S., Abellan, X., Balsamo, G., Bechtold, P., Biavati, G., Bidlot, J., Bonavita, M., De Chiara, G., Dahlgren, P., Dee, D., Diamantakis, M., Dragani, R., Flemming, J., Forbes, R., Fuentes, M., Geer, A., Haimberger, L., Healy, S., Hogan, R. J., Hólm, E., Janisková, M., Keeley, S., Laloyaux, P., Lopez, P., Lupu, C., Radnoti, G., de Rosnay, P., Rozum, I., Vamborg, F., Villaume, S., and Thépaut, J.-N.: The ERA5 global reanalysis, Quarterly Journal of the Royal Meteorological Society, 146, 1999–2049, https://doi.org/https://doi.org/10.1002/qj.3803, 2020.

https://doi.org/10.5194/ar-2025-34
Preprint. Discussion started: 7 November 2025

Kaiser, J. W., Heil, A., Andreae, M. O., Benedetti, A., Chubarova, N., Jones, L., Morcrette, J.-J., Razinger, M., Schultz, M. G., Suttie, M., and van der Werf, G. R.: Biomass burning emissions estimated with a global fire assimilation system based on observed fire radiative power, Biogeosciences, 9, 527–554, https://doi.org/10.5194/bg-9-527-2012, 2012.

Kalivitis, N., Kerminen, V.-M., Kouvarakis, G., Stavroulas, I., Tzitzikalaki, E., Kalkavouras, P., Daskalakis, N., Myriokefalitakis, S., Bougiatioti, A., Manninen, H. E., Roldin, P., Petäjä, T., Boy, M., Kulmala, M., Kanakidou, M., and Mihalopoulos, N.: Formation and growth of atmospheric nanoparticles in the eastern Mediterranean: results from long-term measurements and process simulations, Atmospheric Chemistry and Physics, 19, 2671–2686, https://doi.org/10.5194/acp-19-2671-2019, 2019.

Kirchstetter, T. W., Novakov, T., and Hobbs, P. V.: Evidence That the Spectral Dependence of Light Absorption by Aerosols Is Affected by Organic Carbon, Journal of Geophysical Research: Atmospheres, 109, https://doi.org/10.1029/2004JD004999, 2004.

Kivekäs, N., Massling, A., Grythe, H., Lange, R., Rusnak, V., Carreno, S., Skov, H., Swietlicki, E., Nguyen, Q. T., Glasius, M., and Kristensson, A.: Contribution of ship traffic to aerosol particle concentrations downwind of a major shipping lane, Atmospheric Chemistry and Physics, 14, 8255–8267, https://doi.org/10.5194/acp-14-8255-2014, 2014.

Klimont, Z., Kupiainen, K., Heyes, C., Purohit, P., Cofala, J., Rafaj, P., Borken-Kleefeld, J., and Schöpp, W.: Global anthropogenic emissions of particulate matter including black carbon, Atmospheric Chemistry and Physics, 17, 8681–8723, https://doi.org/10.5194/acp-17-8681-2017, 2017.

Lee, S., Yoon, S.-C., Kim, S.-W., Kim, Y. P., Ghim, Y. S., Kim, J.-H., Kang, C.-H., Kim, Y. J., Chang, L.-S., and Lee, S.-J.: Spectral dependency of light scattering/absorption and hygroscopicity of pollution and dust aerosols in Northeast Asia, Atmospheric Environment, 50, 246–254, https://doi.org/10.1016/j.atmosenv.2011.12.026, 2012.

Lewis, E. R. and Schwartz, S. E.: Sea salt aerosol production: mechanisms, methods, measurements, and models, vol. 152, American geophysical union, 2004.

Martinsson, J., Swietlicki, E., and Stenström, K.: Seasonal Variations of Light-Absorbing properties in Atmospheric Aerosols in Southern Sweden, in: LUCCI Annual Report 2013/2014, 2014.

Masson-Delmotte, V., Zhai, P., Pirani, A., Connors, S., Péan, C., Berger, S., Caud, N., Chen, Y., Goldfarb, L., Gomis, M., Huang, M., Leitzell, K., Lonnoy, E., Matthews, J., Maycock, T., Waterfield, T., Yelekçi, O., Yu, R., and Zhou, B.: IPCC, 2021: Summary for Policymakers, chap. 7, Cambridge University Press, 2021.

Matlab, V.: 9.7. 0.1190202 (R2021a), The MathWorks Inc.: Natick, MA, USA, 2021.

Mogo, S., Cachorro, V. E., Lopez, J. F., Montilla, E., Torres, B., Rodríguez, E., Bennouna, Y., and de Frutos, A. M.: In situ measurements of aerosol optical properties and number size distributions in a coastal region of Norway during the summer of 2008, Atmospheric Chemistry and Physics, 12, 5841–5857, https://doi.org/10.5194/acp-12-5841-2012, 2012.

Müller, T., Laborde, M., Kassell, G., and Wiedensohler, A.: Design and Performance of a Three-Wavelength LED-based Total Scatter and Backscatter Integrating Nephelometer, Atmospheric Measurement Techniques, 4, 1291–1303, https://doi.org/10.5194/amt-4-1291-2011, 2011.

Nordstrøm, C., Ellermann, T., Brandt, J., Christensen, J., Ketzel, M., Massling, A., Bossi, R., Frohn, L. M., Geels, C., Solvang Jensen, S., Nielsen, O.-K., Winther, M., Bech Poulsen, M., Bjært Sørense, M., Skou Andersen, M., and Sigsgaard, T.: Luftkvalitet 2023, Tech. rep., Aarhus Universitet, DCE – Nationalt Center for Miljø og Energ, 2024.

Perrone, M., Romano, S., Genga, A., and Paladini, F.: Integration of optical and chemical parameters to improve the particulate matter characterization, Atmospheric Research, 205, 93–106, https://doi.org/10.1016/j.atmosres.2018.02.015, 2018.

https://doi.org/10.5194/ar-2025-34
Preprint. Discussion started: 7 November 2025

Pisso, I., Sollum, E., Grythe, H., Kristiansen, N. I., Cassiani, M., Eckhardt, S., Arnold, D., Morton, D., Thompson, R. L., Groot Zwaaftink, C. D., Evangeliou, N., Sodemann, H., Haimberger, L., Henne, S., Brunner, D., Burkhart, J. F., Fouilloux, A., Brioude, J., Philipp, A., Seibert, P., and Stohl, A.: The Lagrangian particle dispersion model FLEXPART version 10.4, Geoscientific Model Development, 12, 4955–4997, https://doi.org/10.5194/gmd-12-4955-2019, 2019.

Plejdrup, M., Nielsen, O.-K., and Christensen, J.: Emission scenarios and air quality modelling for residential wood combustion. Impact analysis of measures for small wood burning appliances in Denmark and effect on transport of black carbon to the Arctic, Tech. Rep. Scientific report no. 426, Aarhus University, DCE – Danish Centre for Environment and Energy, Salt Lake City, UT, http://dce2.au.dk/pub/SR426.pdf, 2021.

Pope III, C. A. and Dockery, D. W.: Health effects of fine particulate air pollution: lines that connect, Journal of the air & waste management association, 56, 709–742, https://doi.org/10.1080/10473289.2006.10464485, 2006.

Roldin, P.: EMEP, EUSAAR, GAW-WDCA, 2012, Aerosol light scattering coefficient at Vavihill, data hosted by EBAS at NILU, https://doi.org/10.48597/QGZS-5XKM, 2012.

Sandradewi, J., Prevot, A., Szidat, S., Perron, N., Alfarra, M., Lanz, V., Weingartner, E., and Baltensperger, U.: Using Aerosol Light Absorption Measurements for the Quantitative Determination of Wood Burning and Traffic Emission Contributions to Particulate Matter, Environmental science & technology, 42, 3316–23, https://doi.org/10.1021/es702253m, 2008.

Seinfeld, J. H. and Pandis, S. N.: Atmospheric Chemistry and Physics : From Air Pollution to Climate Change, John Wiley & Sons, 3rd edition edn., 2016.

Stohl, A., Forster, C., Frank, A., Seibert, P., and Wotawa, G.: Technical note: The Lagrangian particle dispersion model FLEXPART version 6.2, Atmospheric Chemistry and Physics, 5, 2461–2474, https://doi.org/10.5194/acp-5-2461-2005, 2005.

Suchánková, L., Mbengue, S., Zíková, N., Šmejkalová, A. H., Prokeš, R., Holoubek, I., and Ždímal, V.: A seven-year-based characterization of aerosol light scattering properties at a rural central European site, Atmospheric Environment, 319, 120 292, https://doi.org/10.1016/j.atmosenv.2023.120292, 2024.

Takemura, T., Nakajima, T., Dubovik, O., Holben, B. N., and Kinne, S.: Single-Scattering Albedo and Radiative Forcing of Various Aerosol Species with a Global Three-Dimensional Model, Journal of Climate, 15, 333–352, https://doi.org/https://doi.org/10.1175/1520-0442(2002)015<0333:SSAARF>2.0.CO;2, 2002.

Tørseth, K., Aas, W., Breivik, K., Fjæraa, A. M., Fiebig, M., Hjellbrekke, A.-G., Lund Myhre, C., Solberg, S., and Yttri, K. E.: Introduction to the European Monitoring and Evaluation Programme (EMEP) and observed atmospheric composition change during 1972–2009, Atmospheric Chemistry and Physics, 12, 5447–5481, https://doi.org/10.5194/acp-12-5447-2012, 2012.

Vignati, E., de Leeuw, G., Schulz, M., and Plate, E.: Characterization of aerosols at a coastal site near Vindeby (Denmark), Journal of Geophysical Research: Oceans, 104, 3277–3287, https://doi.org/10.1029/1998JC900019, 1999.

von der Weiden, S.-L., Drewnick, F., and Borrmann, S.: Particle Loss Calculator – a new software tool for the assessment of the performance of aerosol inlet systems, Atmospheric Measurement Techniques, 2, 479–494, https://doi.org/10.5194/amt-2-479-2009, 2009.

Worm, K.: Coastal zone planning in Denmark, Ocean & Coastal Management, 37, 253–268, https://doi.org/10.1016/S0964-5691(00)89026-2, 1997.

Zhang, Z., Li, J., Che, H., Dong, Y., Dubovik, O., Eck, T., Gupta, P., Holben, B., Kim, J., Lind, E., Saud, T., Tripathi, S. N., and Ying, T.: Long-term trends in aerosol properties derived from AERONET measurements, Atmospheric Chemistry and Physics, 25, 4617–4637, https://doi.org/10.5194/acp-25-4617-2025, 2025.

https://doi.org/10.5194/ar-2025-34
Preprint. Discussion started: 7 November 2025

605 Ångström, A.: On the Atmospheric Transmission of Sun Radiation and on Dust in the Air, Geografiska Annaler, 11, 156–166, https://doi.org/10.1080/20014422.1929.11880498, 1929.